ORIGINAL ARTICLE

Research on temperature action and cracking risk of steel–concrete composite girder during the hydration process

Jiang Liu[1] · Yongjian Liu[1] · Ning Zhang[2] · Zhiyuan Ma[1] · Yongxin Bai[1]

Abstract

Temperature changes due to hydration heat often cause cracks in the early-age concrete deck of steel–concrete composite girder bridges, even before opening to traffic. However, no available methods are provided in current specifications for the thermal effect calculation. To fill this gap, large-scale temperature measurements and fine finite-element model (FEM) analysis were performed on an actual composite girder bridge. Based on the fully validated FEM, a comprehensive parametric study was carried out to establish the spatio-temporal pattern of hydration-caused temperature, including a vertical pattern and an evolutionary pattern. Finally, a simplified method was presented for the thermal stress calculation of composite girders, and a case study was also provided. Measurements showed that temperature differences of concrete deck varied below 5 °C, much smaller than the entire composite section. FEM analysis then suggested that the influence of solar radiation can be basically ignored compared with hydration heat. The spatio-temporal pattern in the form of the coefficient of temperature rise was proposed based on the above findings and parametric study, and the reliability was properly verified with experimental or FEM results. For the final simplified method, the case study demonstrated that it can effectively facilitate the thermal stress calculation of composite girders during hydration process by adopting the proposed spatio-temporal pattern. As such, preliminary curing schemes can be easily selected to control the concrete cracking risk before casting.

Keywords Steel–concrete composite girder · Hydration heat · Temperature distribution · Coefficient of temperature rise · Spatio-temporal pattern · Cracking risk

List of symbols

T	Temperature at the calculated point (°C)
t	Time (h)
ρ	Density (kg/m^3)
c	Specific heat (kJ/kg °C)
λ	Thermal conductivity (kJ/m h °C)
$q(t)$	Rate of hydration heat generated per unit volume (kJ/m^3 h)
$Q(t)$	Accumulated hydration heat (kJ/kg)
Q_∞	Final amount of accumulated hydration heat (kJ/kg)
T_0	Initial temperature (°C)
ω, φ, ξ and ζ	Parameters
W	Amount of cement per unit volume of concrete (kg/m^3)
$T_{r,\infty}$	Final adiabatic temperature rise (°C)
T_s	Temperature of bridge surface (°C)
T_a	Air temperature (°C)
β	Convective coefficient (kJ/m^2 h °C)
v	Wind speed (m/s)
β_e	Equivalent convective coefficient (kJ/m^2 h °C)
δ_i	Thickness of layer i (m)
λ_i	Thermal conductivity of layer i (kJ/m h °C)
β_0	Convective coefficient of the outermost layer (kJ/m^2 h °C)
α	Solar absorptivity
ε	Emissivity
T_c	Curing temperature (°C)
β_t	Convective coefficient of the top surface of deck (kJ/m^2 h °C)
t_c	Thickness of concrete deck (m)
γ	Coefficient of temperature rise (CTR)

✉ Yongjian Liu
liuyongjian@chd.edu.cn

1   School of Highway, Chang'an University, Middle Section of the South Second Ring Road, Xi'an 710064, Shaanxi, China

2   College of Water Resources and Architectural Engineering, Northwest A&F University, Yangling 712100, Shaanxi, China

$\gamma_{c,max}$	Maximum CTR of concrete deck
t_0	Occurring time of maximum CTR
γ_c	Uniform CTR of concrete deck
γ_{sd}	CTR of the bottom flange of steel girder
$\Delta\gamma$	Difference of CTR in steel girder, equals to γ_c minus γ_{sd}
n	Power exponent
h_0	Influence height of concrete hydration heat on steel girder (m)
h_s	Height of steel girder (m)
MS_T and MS_E	Mean squares between groups and within groups
SS_T and SS_E	Sum of squares between groups and within groups
I_m and I_n	Number of groups and cases
α	Significant level
γ_{Tc}	CTR after the hydration heat is over, $\gamma_{Tc} = (T_c - T_0)/T_{r,\infty}$
t_1	Corresponding ages to $\gamma_{c,max}/2$ in ascending stage
t_2	Corresponding ages to $(\gamma_{c,max} + \gamma_{Tc})/2$ in descending stage
p and q	Coefficients
AAE	The average absolute error
RMSE	The root-mean-square error
R^2	Coefficient of determination
t_i	Age of concrete (days)
$\Delta\varepsilon_{tot,i}(y)$	Increment of total axial strains
y_{iG}	Distance from the centroid of composite section to the interface
$\Delta\varepsilon_{0,i}$	Increment of centroidal axial strain
$\Delta\varphi_i$	Increment of curvature
$\Delta\varepsilon_{e,i}$	Increment of elastic strain
$\Delta\varepsilon_{T,i}$	Increment of temperature strain
α_c	Coefficient of thermal expansion of concrete
α_s	Coefficient of thermal expansion of steel
$\Delta T_i(y)$	Vertical distribution of the temperature increment
$\Delta T_{c,i}$	Temperature increment of concrete
ΔN_i	Centroidal axial force
ΔM_i	Moment around the centroidal axis
A_c	Area of concrete deck
A_s	Areas of steel girder
$E_i(y)$	Elastic modulus
$E_{c,i}$	Elastic modulus of concrete
E_s	Elastic modulus of steel
$f_{t,i}$	Tensile strength of concrete
$E_{c,28}$	Elastic modulus of concrete at a 28-day age
$f_{t,28}$	Tensile strength of concrete at a 28-day age
s	Coefficient
y_{cG}	Coordinate of the centroid of concrete deck
$I_{c,0}$	Moments of inertia of concrete deck around the centroidal axis
$I_{s,0}$	Moments of inertia of steel girder around the centroidal axis
f_{td}	Design value of tensile strength (MPa)
$f_{t,k}$	Characteristic value of tensile strength (MPa)

1 Introduction

Concrete hydration is an exothermic reaction that can produce high amounts of heat during curing, especially in the first few days after concreting. Temperature changes due to hydration heat will cause thermal cracks not only in mass concrete structures [1, 2], but also in relatively thin concrete slabs in bridges [3]. During the cooling phase at the end of hydration, contraction occurs in the concrete deck. These cracks develop due to the stud-caused constraint of steel girder on the contraction of concrete deck [4]. Generally, these cracks occur shortly after the concrete casting of deck slabs, even before opening to traffic. As such, not only the early-age performance of concretes but also the service life of composite girder bridges will be adversely affected [5, 6].

To avoid early cracking in concrete decks, effects of hydration should be estimated before concrete placement. In this regard, priority should be given to the temperature distribution of composite girder during hydration process. In situ measurements should be performed on large-scale segments or actual bridges to reflect the actual distribution of the hydration heat temperature of real bridges as much as possible. William et al. [7] instrumented a reinforced concrete deck on a three-span continuous steel girder to measure the temperature development and regressed the linear relationship between temperature changes and stress changes. Subramaniam [8] studied the variation of temperature rise in the concrete deck and steel girder by field test on a composite girder during hydration process. Choi et al. [9, 10] execute a model test on a simple-supported composite girder at a depth of 0.76 m and a length of 8.0 m to investigate the characteristic of temperature distribution in the concrete deck and steel girder. All these measurements suggested that the temperature distribution of composite girder was exactly uneven during hydration process. Also, obvious temperature differences were observed between steel and concrete. However, temperature measurements are often limited in number of measuring points, making it difficult to obtain a spatially continuous bridge temperature field, with which the thermal effect cannot be directly calculated. The most comment used method of fine calculation is the unidirectional thermo-mechanical coupling analysis, in which the temperature

distribution is firstly calculated and a mechanical analysis is secondly performed. Faria et al. [11] and Huang et al. [12] calculated the thermal effect of a restrained concrete slab and a massive concrete pier during concrete hydration successfully by using this method, respectively. Other than that, Lee et al. [13] employed the microplane model of hydration heat and simulated the temperature field and the cracking patterns of concrete structures with early age. Zhang et al. [14] applied this method in the calculation of temperature and stress fields of a concrete pylon under solar radiation. The unidirectional thermo-mechanical coupling analysis is detailed but technically difficult, time-consuming and laborious, thus not convenient for direct applications in engineering.

In current specification system, such as AASHTO LRFD [15] and Eurocode 1 [16], the uniform temperature caused by air temperature changes and the temperature gradient caused by solar radiations in the bridge service stage are clearly specified. However, no applicative temperature patterns are available in current specifications for the thermal effect calculation of composite girders during hydration process, during which the concrete deck is more prone to cracking when the early-age concrete is inappropriately cured. When solar radiation acts on the top surface of bridges, temperatures are generally nonlinearly distributed within the top range of 0.3–0.5 m [17, 18]. Scholars have proposed several temperature gradient patterns, including polyline forms [15, 16], multiple parabolic forms [19–25] and exponential forms [22], for concrete, steel and composite girder bridges. Among them, Priestley [18] proposed a temperature gradient

pattern with a 5th parabolic curve for concrete box girders. Li et al. [26] measured a deep concrete girder and proposed a third parabolic temperature gradient pattern. For steel girders, Tong et al. [27] established a similar temperature gradient pattern based on Priestley's finding. Liu et al. [19, 28] established the 2nd–4th parabolic gradient patterns for composite girders. Additionally, in the calculation of solar-caused thermal effect, only the most unfavorable pattern needs to be concerned and the time-dependent characteristic is usually ignored [15, 16, 19, 21].

Influenced by hydration heat of composite girders, significant distinctions of thermal effect calculation exist between hydration stage and service stage [8–10, 22]. Firstly, the source position and form of internal hydration heat are totally different from solar heat source, causing quite different temperature distribution patterns. In addition, the time-dependent characteristic needs to be concerned in the thermal effect calculation during hydration process, because not only the mechanical properties of concrete but also the hydration temperature develops fast at the early age [23]. Therefore, the calculation of hydration heat-caused thermal effect is a spatio-temporal problem, and relevant conclusions of the solar-caused temperature actions and thermal effects are not exactly suitable for that.

This study focuses on developing a suitable spatio-temporal pattern of hydration heat temperature for the thermal effect calculation of composite girders. Figure 1 shows the flowchart of the methodology. Large-scale temperature measurements were firstly performed on an actual composite girder bridge, and the measured results were used for the

Fig. 1 Flowchart of methodology
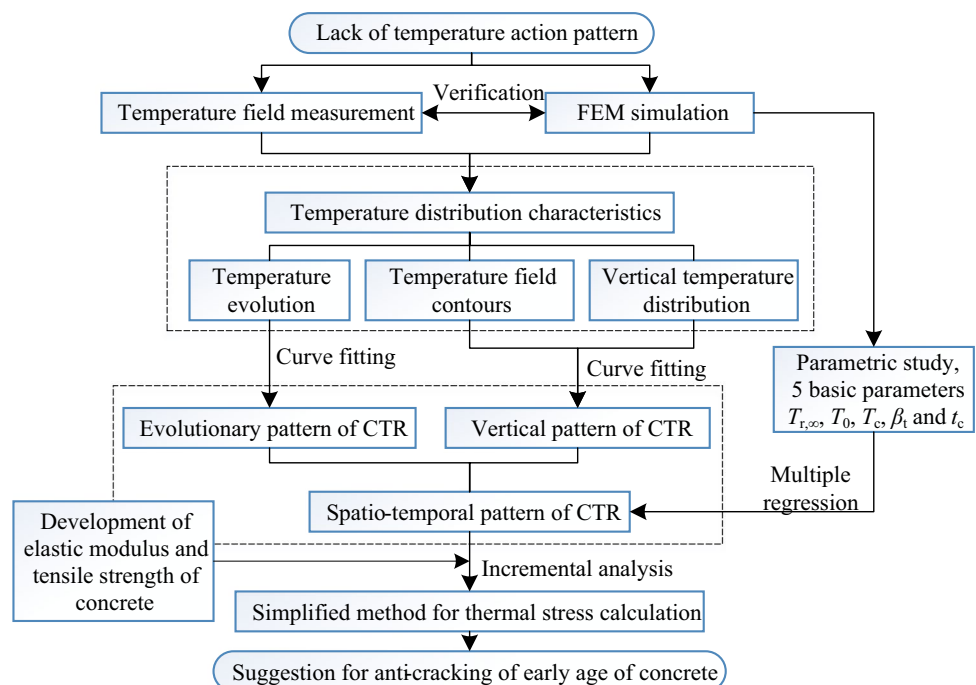
verification of FEM method. Then, a comprehensive parametric study was carried out involving five basic parameters including final adiabatic temperature rise $T_{r,\infty}$, initial temperature T_0, curing temperature T_c, convective coefficient β_t and deck thickness t_c. After that, a spatio-temporal pattern was proposed in the form of the coefficient of temperature rise (CTR) by curve fitting. Through multiple regression analysis, parametric study results were used to establish a series of empirical formulae to predict the key coefficients in the pattern. Finally, by adopting the proposed pattern, a simplified method was presented to facilitate the thermal stress calculation of composite girders and cracking risk of concrete decks.

2 Hydration temperature field measurement

2.1 Tested composite girder

A field measurement was performed to investigate the temperature distribution of a composite girder bridge during hydration process. The bridge is situated at a mountainous area with an altitude of 491 meters, where the geographic coordinates are 108.51° E and 32.98° N. The composite girder with a span of 20 meters is grouped by a concrete deck lying on two longitudinal steel girders and three transverse steel beams. Figure 2 shows the layout of mid-span section. The height and width of the girder are 1.17 m and 3.70 m, respectively. The concrete deck has a general thickness of

0.19 m and a thickened part of 0.27 m. Reinforcement ratios of concrete deck in longitudinal and transverse are 0.85% and 2.54%, respectively. The two longitudinal steel girders have a same height of 0.90 m, and the spacing distance between each other is 2.0 m. Three I-shaped steel beams with a height of 0.25 m were evenly set on the webs of steel girders for cross connection. Shear connectors of 22 mm diameter were used in the interfacial region. C50 concrete was adopted for the concrete deck. Table 1 shows the mix proportion and corresponding thermal parameters of the C50 concrete. A type of P.O.52.5 Portland cement was used by 440 kg/m³, and the water–cement ratio is 0.35. In addition, polycarboxylate superplasticizer was used as water-reducing agent to improve the fluidity and workability of concrete, and type SY-HEA anti-cracking agent was employed to provide micro-expansion and fibers to prevent concrete cracking.

2.2 Sensor arrangement

For the accurate temperature measurement, 71 temperature sensors of DS18B20 digital thermometers were installed on the composite girder. The section 0.5 m away from the mid-span section was selected as the experimental section to avoid the interference of cross-beam on sensor arrangement. Among the 71 temperature sensors, 47 of them were embedded into the concrete deck, while 24 of them were attached on the web surface of steel girder. Figure 3 shows the arrangements of these sensors. Additionally, environmental parameters, including air temperature, air humidity,

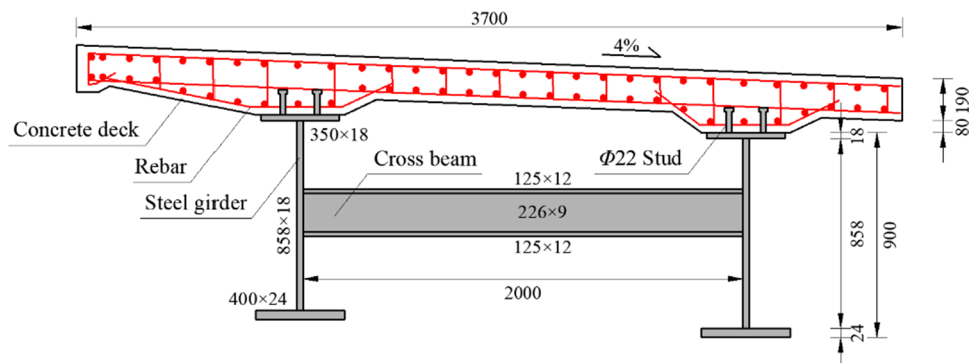**Fig. 2** Layout of mid-span section (unit: mm)

Table 1 Mix proportion and thermal parameters of each component in C50 concrete

Item	Water	Cement	Sand	Gravel	Water reducing agent	Anti-cracking agent
Unit weight (kg/m³)	154	440	651	1159	45	9.7
Percentage (%)	6.30	17.89	26.47	47.12	1.83	0.39
Specific heat (kJ/kg °C)	4.187	0.456	0.699	0.749	/	/
Conductivity (kJ/m h °C)	2.16	4.446	11.129	14.528	/	/

wind speed, wind direction and solar radiation, were also recorded by a weather station nearby. The monitoring data from both the girder and external environment were obtained simultaneously at a time interval of 60 s. To reduce the jaggedness and increase the smoothness of the original collected data, the experimental data shown in the subsequent figures were all converted to hourly resolution.

2.3 Experimental program

Timber formworks were used for casting concrete. The concrete pouring, followed by an artificial vibration, was started at 1:30 p.m., and finished at 4:00 p.m. on December 27th. The concrete molding temperature was 13 °C, which could be considered as a uniform initial temperature of concrete deck. At one hour after casting, the top surface of concrete deck was covered by asbestos cloth for heat and moisture insulation. In addition, several hot water-heating boilers were set under the girder for continuous heat and moisture preservation. The asbestos cloth and wood formworks were both stripped at 48 h after concrete casting. The composite girder was supported by concrete blocks at 20–40 cm heights to allow natural ventilation for the bottom of steel girders. Experimental photographs are shown in Fig. 4.

2.4 Measured meteorological parameters

Figure 5 shows the variations of air condition within 72 h after concrete casting. The daily fluctuation of air temperature could reach a maximum range of 16.2 °C when the lowest temperature appeared at − 1.31 °C. In the contrast, curing temperature under the asbestos cloth held in a relatively

stable range within 48 h after concrete casting. The curing temperature had an average value of 14.2 °C and a fluctuation value of 6.5 °C during the curing time with asbestos cloth. The air humidity had a maximum value of 70.15%. The flow of solar radiation into bridge deck was relatively small due to a rainy weather in the first two days, and the radiation increased to a maximum value of 1704 kJ/h m^2 in the next two sunny days. There was not an obvious trend of wind speed during the hydration process, and the maximum wind speed was 3.3 m/s.

3 Finite element analysis

3.1 Heat transfer theory

3.1.1 Heat transfer equation

Concrete under the hydration reaction can be regarded as a continuous uniform medium with an internal heat source and a transient temperature field, which can be simulated with finite-element method. The general partial differential equation governing the heat conduction can be presented as [17]:

$$\rho c \frac{\partial T}{\partial t} = \lambda \left(\frac{\partial^2 T}{\partial x^2} + \frac{\partial^2 T}{\partial y^2} + \frac{\partial^2 T}{\partial z^2} \right) + q(t) \tag{1}$$

where T is the temperature at the calculated point (°C); t is time, h; ρ is density (kg/m^3); c is specific heat (kJ/kg °C); λ is thermal conductivity (kJ/m h °C); $q(t)$ is the rate of hydration heat generated per unit volume (kJ/m^3 h), which mainly depends on the cement type.
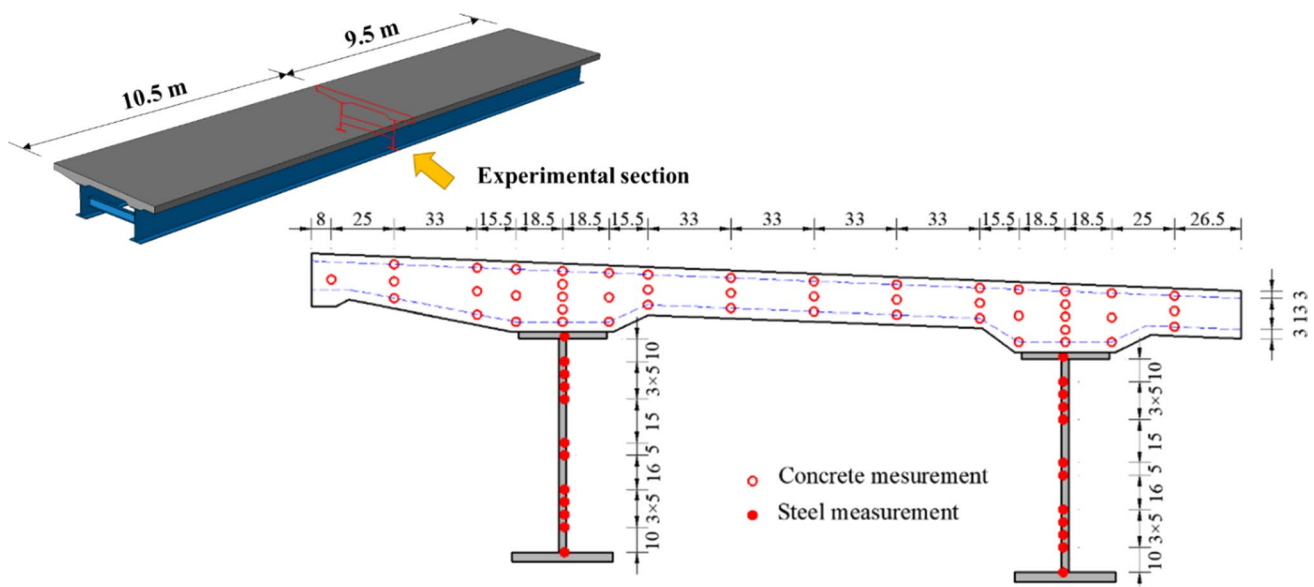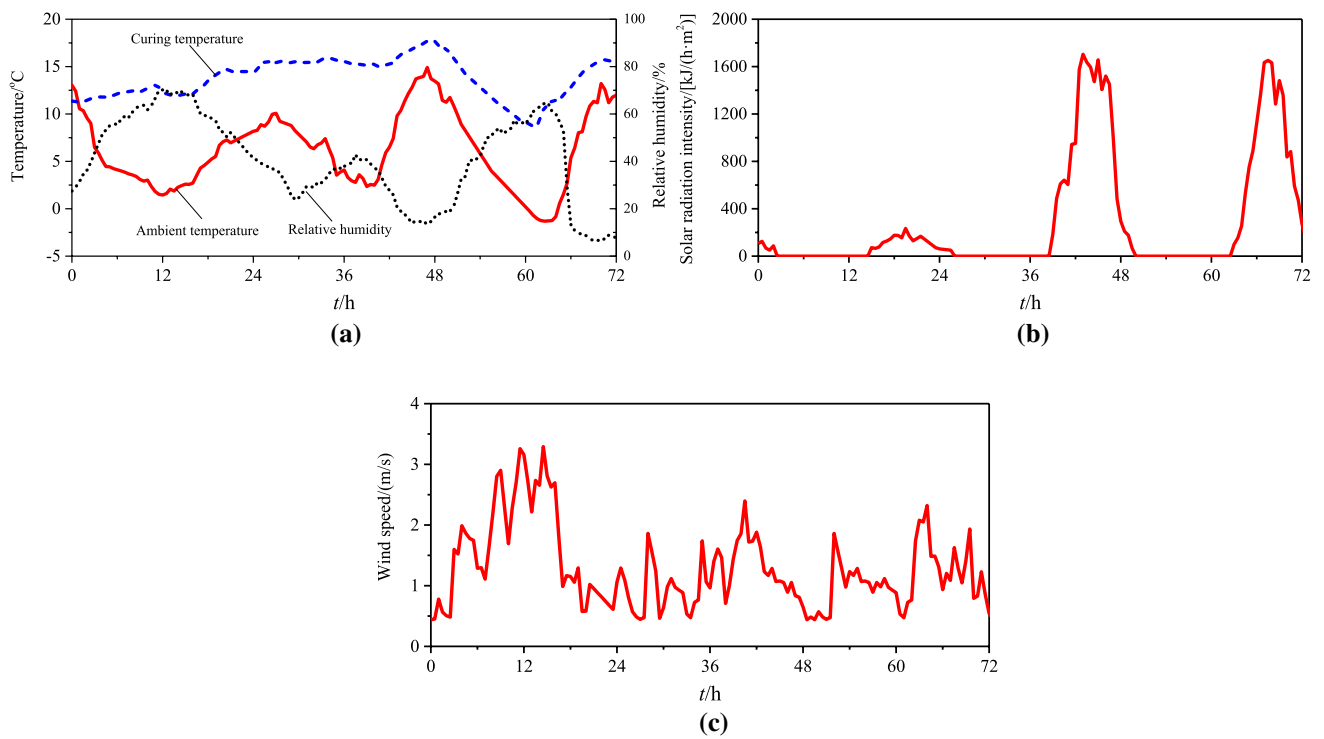

Fig. 3 Arrangement of temperature sensors (unit: cm)

Fig. 4 Experimental photographs: **a** reinforcement assembly, **b** temperature sensors arrangement in concrete deck, **c** temperature sensors arrangement in steel girder, **d** mobile weather station, **e** concrete cast, **f** concrete curing with asbestos cloth and **g** constructed composite girder

Fig. 5 Meteorological parameters within 72 h during hydration: **a** air temperature and humidity, **b** solar radiation intensity and **c** wind speed

3.1.2 Hydration heat

During hydration reaction, the rate of exothermic hydration heat gradually slows down, and the accumulated hydration heat gradually increases to the final hydration heat, which is the end of hydration reaction. Based on the global kinetic law of reaction, a hydration heat model was present in research [24]. This model can take the initial temperature of concrete into consideration and thus has been used in the hydration heat temperature calculation of different concrete structures [24, 25]. The model is presented as

$$Q(t) = Q_\infty \exp\left\{-\omega\left[2\varphi\exp\left(\zeta T_0\right)\frac{t}{60}\right]^{-\xi}\right\} \tag{2}$$

where $Q(t)$ is the accumulated hydration heat (kJ/kg); Q_∞ is the final amount of accumulated hydration heat (kJ/kg); T_0 is the initial temperature of concrete; t is the concrete age in minute; ω, φ, ξ and ζ are parameters.

Based on the above model, the rate of hydration heat can be calculated by

$$q(t) = W\frac{dQ}{dt} \tag{3}$$

where W is the amount of cement per unit volume of concrete (kg/m^3).

The final adiabatic temperature rise is completely converted from the heat generated by hydration reaction under an adiabatic condition, and it is related to the cement type and the concrete mix proportion [29]. It can be calculated by

$$T_{r,\infty} = \frac{Q_\infty W}{c\rho} \tag{4}$$

where $T_{r,\infty}$ is the final adiabatic temperature rise (°C).

3.1.3 Boundary condition

The temperature difference between bridge surface and air environment results in heat loss or gain by a convective

boundary condition, which is governed by Newton's law of cooling [17] and can be expressed as

$$-\lambda\frac{\partial T}{\partial n} = \beta\left(T_s - T_a\right) \tag{5}$$

where T_s and T_a are the temperatures of bridge surface and air, respectively (°C); β is convective coefficient between the bridge surface and the surrounding air (kJ/m^2 h °C). The β of smooth surfaces can be calculated with wind speed by [24]

$$\beta = 18.46 + 17.36v^{0.883} \tag{6}$$

where v is wind speed (m/s).

Formworks or insulation layers are often used for the shaping and curing of early-age concrete. The equivalent convective coefficient β_e of the outer surface of formworks or insulation layers can be calculated by [29]

$$\beta_e = \frac{1}{1/\beta_0 + \sum\left(\delta_i/\lambda_i\right)} \tag{7}$$

where δ_i is the thickness of layer i (m); λ_i is the thermal conductivity of layer i (kJ/m h °C); β_0 is the convective coefficient between the outermost insulation layer and the surrounding air (kJ/m^2 h °C).

## 3.2 Finite-element model (FEM) development

3.2.1 FEM

Finite-element program ABAQUS 6.14 was used for the 3D heat transfer simulation of composite girder during hydration process. Figure 6 shows the FEM, in which all the components were meshed with the structured technique provided in ABAQUS. An 8-node linear heat transfer brick element, DC3D8, with a shape of hexahedron was employed for the simulation of concrete deck. A 4-node linear heat transfer shell element, DS4, with a shape of quadrangle was employed for the simulation of steel girder. The size of all the elements was set around 50 cm; as such, the node

Fig. 6 3D FEM of composite girder
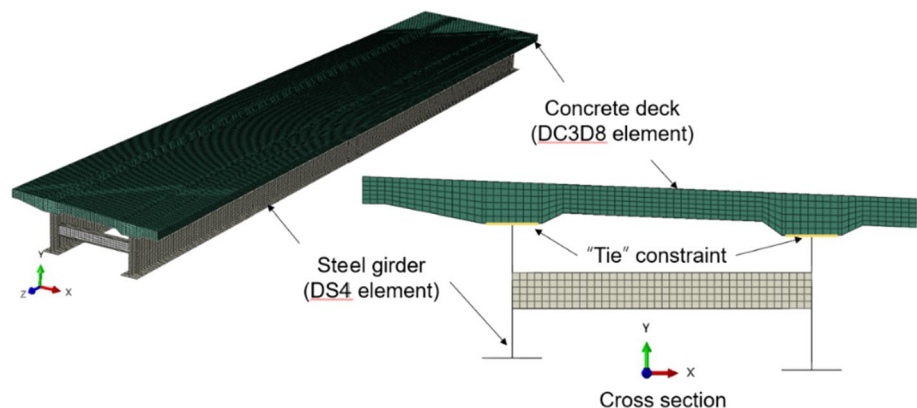
Table 2 Thermal properties of concrete and steel

Thermal property	Concrete	Steel
Density ρ (kg/m^3)	2399.66	7850.00
Conductivity λ (kJ/m h °C)	10.72	198.00
Specific heat c (kJ/kg °C)	0.88	0.475
Solar absorptivity α	0.55	0.60
Emissivity ε	0.85	0.80
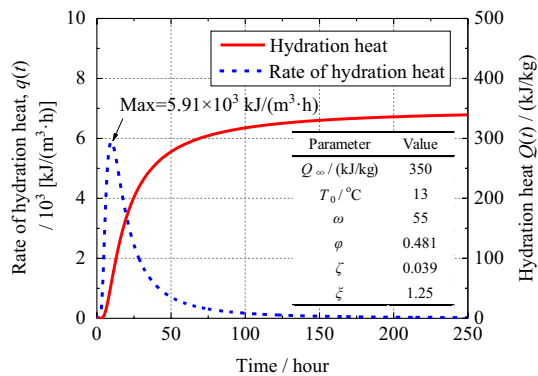
Fig. 7 Development of concrete hydration heat

positions in the depth of concrete deck and steel girder can match the experimental arrangement of temperature sensors. The interfacial relationship between deck and steel girder was approximately modeled as "tie constraints," so that the temperature and heat flux are continuous at the interface [21]. The thermal properties of concrete and steel are listed in Table 2. The density, conductivity and specific heat of concrete were valued as the average of each component with weights of the mix proportion in Table 1. The thermal properties of steel were referred to existing researches [19, 21, 28].

3.2.2 Hydration heat

A type of P.O.52.5 Portland cement was used in the deck of the test composite girder, and the corresponding final amount of accumulated hydration heat is 350 kJ/kg [29]. The rate of hydration heat was calculated with Eqs. (2) and (3), in which the coefficients ω, φ, ζ and ξ were taken as 55, 0.481, 0.039 and 1.25 [24]. Figure 7 shows the development of hydration heat. The maximum rate of hydration heat reached 5.91×10^3 kJ/m^3 h.

3.2.3 Initial temperature and boundary conditions

In the FEM, the hydration temperature field was calculated every half hour for more accurate and detailed simulation results. The initial temperature was determined by

the measured temperature, 13 °C for concrete deck, and 12 °C, 10 °C and 9 °C for the top flange, web and bottom flange, respectively. Temperatures of cross-beams were considered to be same as the web temperature.

The tested composite girder was located in a sulci form terrain. Blocked by concrete deck and the terrain, steel girders were not exposed to sunrays during the test period. Thus, the effect of solar radiation on the top surface of concrete deck was only taken into consideration. The recorded solar radiation intensity, as shown in Fig. 5b, was inputted in the FEM, and the solar absorptivity was taken as 0.4 for ordinary concrete surface [30] and 0.3 for white asbestos cloth [31].

The wind speed is not considered during the period when the composite girder was covered by the asbestos cloth at the first 48 h. The thermal conductivity and thickness of timber formworks are 0.837 kJ/m h °C and 1.5 cm, respectively. Then, it can be calculated with Eq. (7) that the equivalent convective coefficient of timber formworks is 13.871 kJ/m^2 h °C. After the asbestos cloth and formworks was stripped, the convective coefficient was calculated with Eq. (6) by taking the wind speed into account.

4 Temperature results analysis

4.1 Temperature evolutions

Figure 8 shows the FEM and experimental temperature evolutions. Well agreements were shown between FEM and experimental results. Only the experimental web temperatures in S7 and S19 are relatively larger than FEM results because of the aforementioned heating boilers, which were not considered in the FEM. It can be also seen that temperature evolutions on the left and right sides are basically consistent. Concrete temperatures elevate significantly faster than the steel girder. Taking the left side as an example, at about 27 h, the center temperature in concrete deck reaches the first peak, 31.2 °C. At about 42 h to 44 h, the concrete temperature drops to the first valley, 27.3 °C. Subsequently, heated by solar radiation, the concrete temperatures elevate to another slight peak, 27.8 °C, at about 47 h. For steel girder, the heat flow is transmitted from the concrete deck and dissipated by air convection. The top flange is in contact with the concrete deck, and the temperature varies in similar trend with the concrete deck, whereas, with much slower elevation rate. The first measured peak of the top flange is 27.8 °C. The bottom flange is farthest away from the concrete deck. Thus, the temperature is mainly affected by and consistent with the variation of the curing temperature instead of hydration heat.
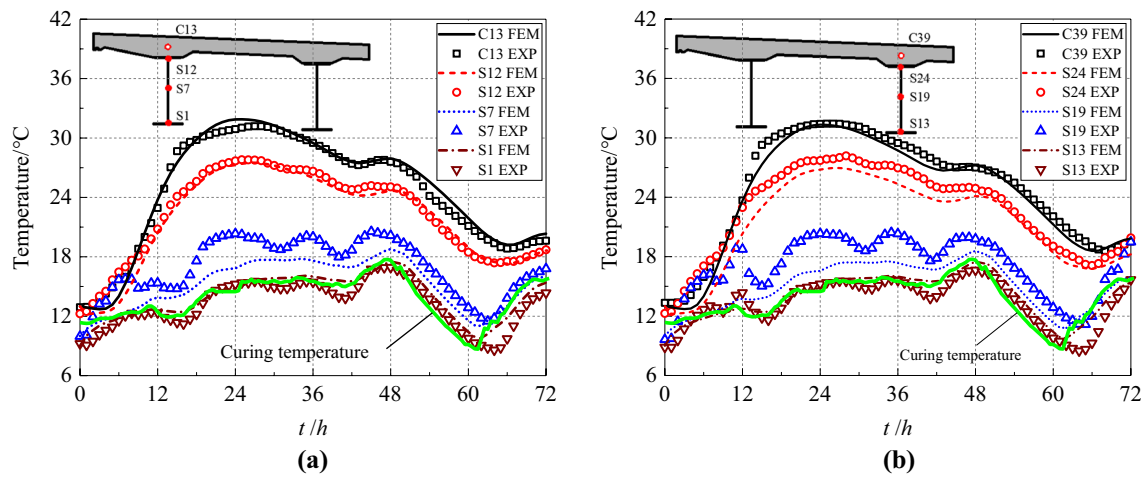
Fig. 8 Temperature evolution of composite girder during hydration process: **a** left side and **b** right side

4.2 Temperature field contours

From the peaks and valleys in Fig. 8, the temperature evolution can be divided into the following four phases:

- Phase I: the warming phase by hydration heat, during about 0–27 h.
- Phase II: the first cooling phase, during about 27–43 h.
- Phase III: the warming phase by solar radiation, during about 43–47 h.
- Phase IV: the second cooling phase, after 47 h.

Figure 9 shows the comparison of experimental and FEM temperature field contours in typical times. These experimental contours were obtained by interpolating the measured temperature data through the Delaunay triangulation algorithm and calculating the weight of each temperature data with Thiessen polygons [22]. The comparison further suggests the accuracy of the FEM. In addition, these contours show that the temperature distribution is relatively uniform in the transverse direction of concrete deck, while large temperature difference exists in the vertical direction of composite girder.

Fig. 9 Temperature field contours: **a** experimental results and **b** FEM results
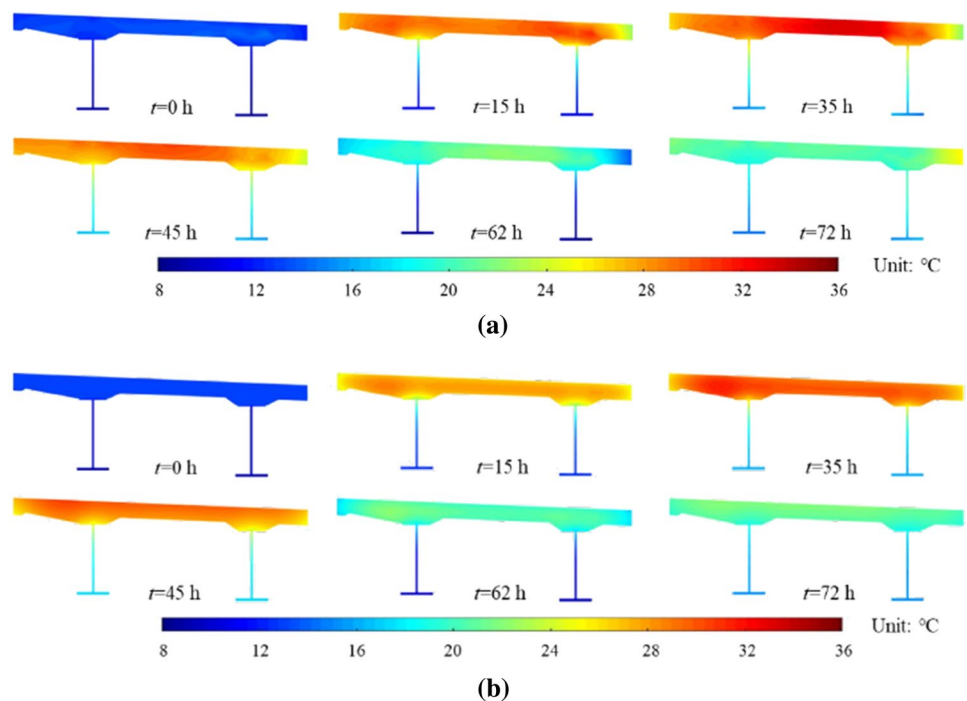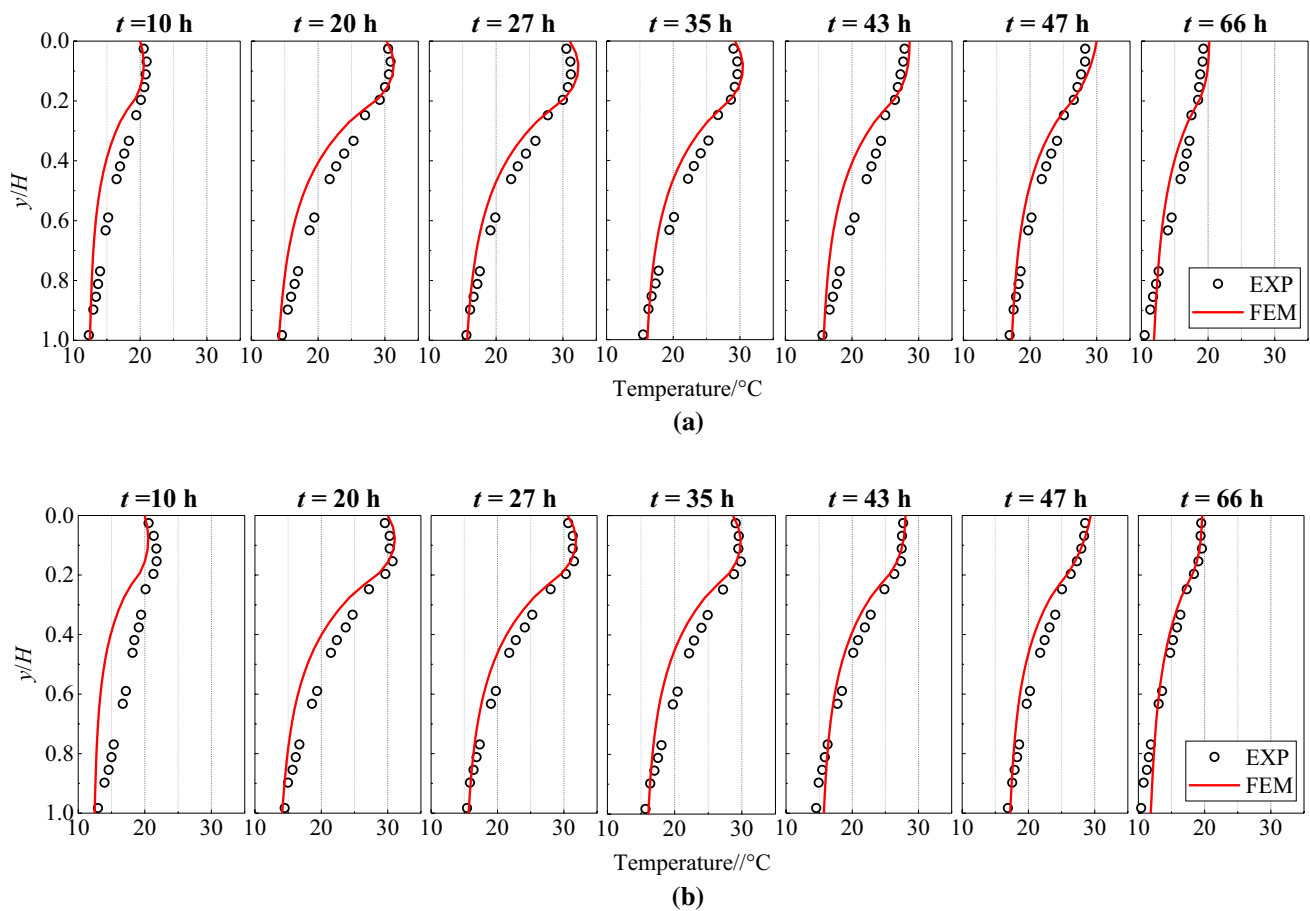
Fig. 10 Vertical temperature distribution of the composite girder: **a** left side and **b** right side

4.3 Vertical temperature distribution

Figure 10 shows the experimental and FEM vertical temperature distributions of composite girder. The effect that the aforementioned hot water-heating boilers made the experimental web temperatures higher than the FEM results was also presented in the figures. Overall, temperatures of concrete deck were significantly higher and more uniformly distributed than the steel girder due to the effect of hydration heat. In Phase I and Phase II, hydration heat made the temperature at the center of the bridge deck the highest and gradually decreasing in both sides. While in phase III and phase IV, the effect of solar radiation gradually emerged, causing the temperature at the top of concrete deck to be highest and gradually decreasing downward. Temperatures of steel girders were the highest at the top flange contacted with concrete deck and gradually decreased to the lowest at the bottom flange, which is farthest from the heat source.

Figure 11 shows the experimental and FEM vertical temperature difference (VTD) of composite girder and concrete deck. Well agreements are also shown between experimental and FEM results. Experimental results suggest that VTD
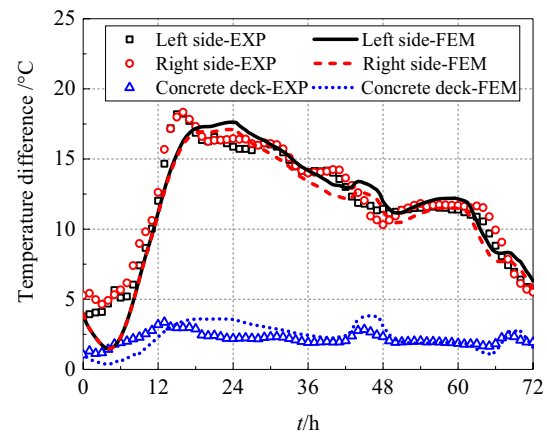

Fig. 11 Evolutions of the vertical temperature difference

of the composite girder varied slowly within about 5 °C in the first five hours and then rapidly increased to the peak of 18.28 °C at 16 h. Subsequently, the VTD decreased gradually, increased slightly due to solar radiation and finally decreased again. The VTD of concrete deck varied similarly

to the composite girder, but consistently within 4 °C, much less than the VTD of the composite girder, throughout the hydration process.

Hydration heat, solar radiation and air convection are the main factors affecting the temperature distribution of the composite girder during the hydration process. With FEM, the effects of above three factors on temperature change in the four phases were quantitatively analyzed, as shown in Fig. 12. In Phase I, the ratio of the effects of hydration heat, solar radiation and air convection on the temperature change of concrete deck is 32.0:1:− 15.5,
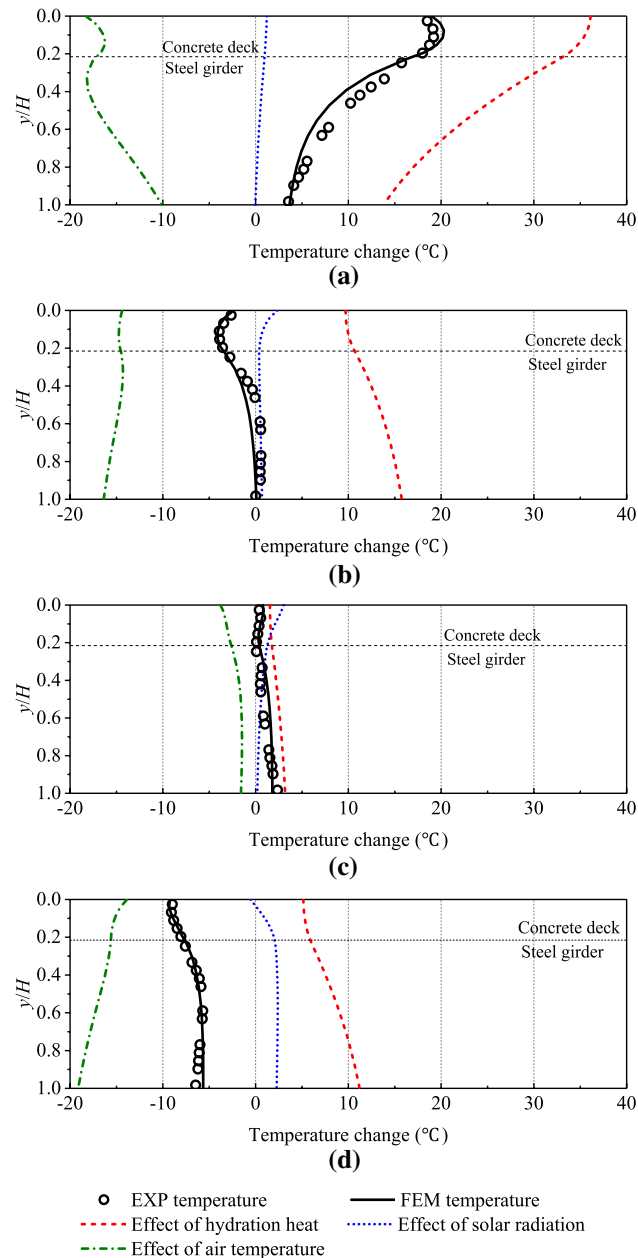
Fig. 12 Vertical distribution of temperature changes in: **a** phases I, **b** phase II, **c** phase III, and **b** phase IV

indicating that the composite girder was mainly warmed by concrete hydration heat and relatively cooled by air convection. In phase II, the effect ratio changes to 10.2:1:− 14.8. The cooling effect of air convection gradually exceeds the warming effect of hydration heat. In phase III, the effect ratio turns into 0.8:1:− 1.5. The effect of solar radiation becomes larger than the hydration heat. However, the temperature change in this phase is very small. In phase IV, the effect ratio becomes 5.4:1:− 14.9. The effect of air convection dominates the temperature decreasing of the composite girder, especially the steel girder. Overall, it is hydration heat and air convection that dominate the temperature change of composite girder, while the influence of solar radiation can be basically ignored.

5 Parametric study

5.1 Parameters

The verified FEM can be used to perform a parametric study to investigate the influence of various parameters on the temperature distribution. A2D FEM, which was simplified from and proved to have the same accuracy as the verified 3D FEM, was used in the parametric study for an efficient calculation. A 4-node linear heat transfer element, DC2D4, with a shape of quadrangle was employed for the simulation of concrete deck and steel girder in 2D FEM. The element size was controlled same with the 3D FEM. The following five basic parameters are involved:

- **Final adiabatic temperature rise of concrete $T_{r,\infty}$** The accumulated hydration heat Q_∞ of ordinary cement ranges from 250 to 370 kJ/kg [29], and the amount of cement W commonly used for concrete deck ranges from 350 to 500 kg/m³ [32]. Therefore, the practical engineering range of $T_{r,\infty}$ is set about 40 to 85 °C according toEq. (4).
- **Initial temperature T_0** "*Code for construction of concrete structures*" *GB 506666-2011* [32] stipulates that the molding temperature of concrete should not be higher than 35 °C and lower than 5 °C. Thus, T_0 is set as 5–35 °C.
- **Curing temperature T_c** In terms of T_0, the parametric range of T_c is also set as 5–35 °C.
- **Convective coefficient of the top surface of concrete deck β_t** β_t reflects the curing condition of the top surface of concrete deck. For a bare surface and a curing condition of 1.5 cm plastic foam + 3 cm straw, β_t equals to 18.5 kJ/m² h °C and 4.4 kJ/m² h °C, respectively. Thus, the parametric range of β_t is set as 5–20 kJ/m² h °C.

- **Thickness of concrete deck t_c** For short and medium span composite girder bridges, t_c commonly ranges from 0.2 to 0.5 m [33].

The above five basic parameters are considered to be the main factors determining the hydration process of concrete deck. These parametric ranges are all set according to practical applications, and the specific values assigned to each parameter are listed in Table 3. For conditions of natural or covering curing, the difference between T_c and T_0 generally does not exceed 10 °C, which can reduce some parameter combinations. As such, the total number of models is reduced to 640. Additionally, in the 2DFEM, T_c is simplified as a constant that does not vary with time. Although it is different from the actual curing condition, this simplification here is to realize a large-scale parametric study.

5.2 Coefficient of temperature rise (CTR)

In the parametric study, a non-dimensional parameter of the coefficient of temperature rise (CTR) was defined as the ratio of actual temperature rise $(T - T_0)$ to the final adiabatic temperature rise $T_{r,\infty}$ and can be calculated by

$$\gamma = \frac{T - T_0}{T_{r,\infty}} \tag{8}$$

where γ is the CTR, which can reflect the actual temperature evolution of concrete deck in an actual engineering curing condition rather than adiabatic condition. In the subsequent results of parametric study, effects of parameters on the maximum CTR of concrete deck $\gamma_{c,max}$ and the corresponding occurring time t_0 were discussed.
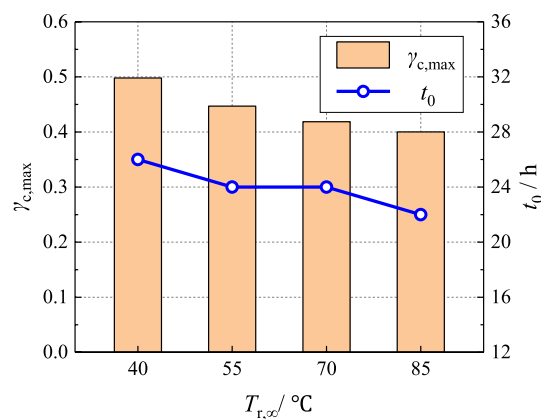
5.3 Results and discussion

5.3.1 Effects of $T_{r,\infty}$

Figure 13 shows the effects of $T_{r,\infty}$ on $\gamma_{c,max}$ and t_0 for the parametric case $T_0 = 15$ °C, $T_c = 25$ °C, $\beta_t = 10$ kJ/m² h °C and $t_c = 0.3$ m. Results indicate that the increase of $T_{r,\infty}$ values leads to decreasing trends of $\gamma_{c,max}$, which means that the higher the adiabatic temperature rise, the

Table 3 Parameters for parametric study

| Level	$T_{r,\infty}$ (°C)	T_0 (°C)	T_c (°C)	β_t (kJ/ m² h °C)	T_c (m)
1	40	5	5	5	0.2
2	55	15	15	10	0.3
3	70	25	25	15	0.4
4	85	35	35	20	0.5

Fig. 13 Effects of $T_{r,\infty}$ on $\gamma_{c,max}$ and t_0 for the parametric case $T_0 = 15$ °C, $T_c = 25$ °C, $\beta_t = 10$ kJ/m² h °C and $t_c = 0.3$ m

less thorough the hydration heat development of concrete under actual engineering conditions. For t_0, a similar effect trend was also observed.

5.3.2 Effects of T_0

Figure 14 depicts the effects of T_0 on $\gamma_{c,max}$ and t_0 for the parametric case $T_{r,\infty} = 70$ °C, $T_c = 25$ °C, $\beta_t = 10$ kJ/m² h °C and $t_c = 0.3$ m. Not only $\gamma_{c,max}$ but also t_0 were observed to decrease with the increase of T_0. When T_0 is less than T_c, part of the contribution of temperature rise comes from air convection. On the contrary, when T_0 is greater than T_c, the temperature drop generated by air convection will neutralize some of the temperature rise, thus lowering the hydration heat temperature rise. In addition, the influence of T_0 on t_0 is nearly linear.
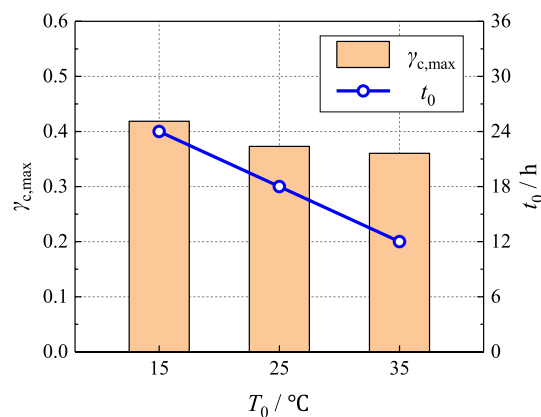
Fig. 14 Effects of T_0 on $\gamma_{c,max}$ and t_0 for the parametric case $T_{r,\infty} = 70$ °C, $T_c = 25$ °C, $\beta_t = 10$ kJ/m² h °C and $t_c = 0.3$ m
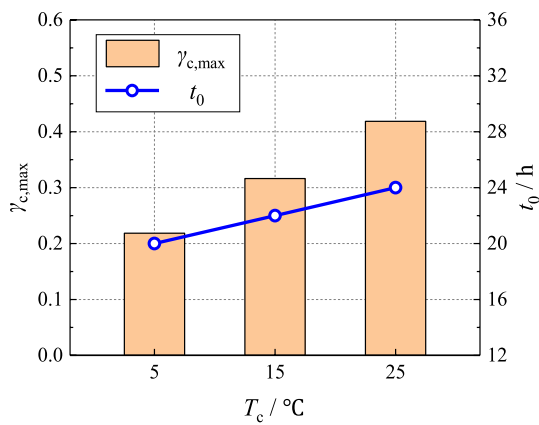
Fig. 15 Effects of T_c on $\gamma_{c,max}$ and t_0 for the parametric case $T_{r,\infty} = 70$ °C, $T_0 = 15$ °C, $\beta_t = 10$ kJ/m^2 h °C and $t_c = 0.3$ m

5.3.3 Effects of T_c
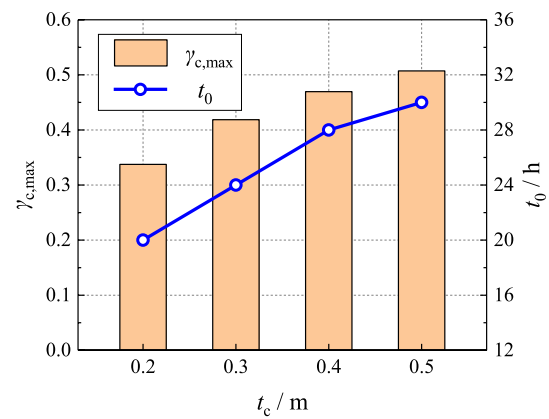
Figure 15 illustrates the effects of T_c on $\gamma_{c,max}$ and t_0 for the parametric case $T_{r,\infty} = 70$ °C, $T_0 = 15$ °C, $\beta_t = 10$ kJ/ m^2 h °C and $t_c = 0.3$ m. It was depicted that both $\gamma_{c,max}$ and t_0 increase linearly with the increase of T_c. This influence characteristics is similar with T_0, which has been explained before.

5.3.4 Effects of β_t

The effects of β_t on $\gamma_{c,max}$ and t_0 for the parametric case $T_{r,\infty} = 70$ °C, $T_0 = 15$ °C, $T_c = 25$ °C and $t_c = 0.3$ m were depicted in Fig. 16. With the increase of β_t, linear drop trends were observed both in $\gamma_{c,max}$ and t_0. In other words, the gradually deteriorating curing conditions accelerate the convection, which reduces and delays the maximum concrete temperature rise.
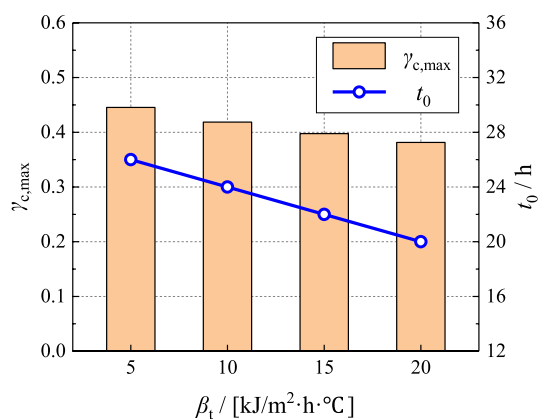
Fig. 16 Effects of β_t on $\gamma_{c,max}$ and t_0 for the parametric case $T_{r,\infty} = 70$ °C, $T_0 = 15$ °C, $T_c = 25$ °C and $t_c = 0.3$ m

Fig. 17 Effects of t_c on $\gamma_{c,max}$ and t_0 for the parametric case $T_{r,\infty} = 70$ °C, $T_0 = 15$ °C, $T_c = 25$ °C, and $\beta_t = 10$ kJ/m^2 h °C

5.3.5 Effects of t_c

The effects of t_c on $\gamma_{c,max}$ and t_0 for the parametric case $T_{r,\infty} = 70$ °C, $T_0 = 15$ °C, $T_c = 25$ °C and $\beta_t = 10$ kJ/m^2 h °C are illustrated in Fig. 17. As the increasing t_c increases the mass of concrete deck, elevating trends of $\gamma_{c,max}$ and t_0 were observed with the increase of t_c.

5.3.6 Analysis of Variance (ANOVA)

Based on the results of above parametric study, ANOVA was employed to analyze the significance of the effect of each parameter on $\gamma_{c,max}$ and t_0. F-test was used to accept or reject the null hypothesis that the means of the different groups are the same at a stated level of significance. F value can be calculated by [34]

$$F = \frac{MS_T}{MS_E}, \quad MS_T = \frac{SS_T}{I_m - 1}, \quad MS_E = \frac{SS_E}{I_n - I_m} \tag{9}$$

where MS_T and MS_E are the mean squares between groups and within groups, respectively; SS_T and SS_E are the sum of squares between groups and within groups, respectively; I_m is the number of groups; I_n is the total number of cases. For a given significant level α, if $F \geq F_{1-\alpha}(I_m - 1, I_n - I_m)$, the F-test will reject the null hypothesis, which means there are serious differences between the means of groups.

In this ANOVA, I_m equals to 4 and I_n equals to 640. The α was selected as 0.05. Then $F_{0.95}(3, 636)$ was calculated to be 2.6. Figure 18 shows the significant analysis of parameters. It can be seen that all the F values of parameters were larger than 2.6, suggesting significance effects on both $\gamma_{c,max}$ and t_0. Additionally, among these parameters, t_c had the greatest influence on $\gamma_{c,max}$, T_0 had the greatest impact on t_0, and $T_{r,\infty}$ has the poorest effects on both $\gamma_{c,max}$ and t_0.
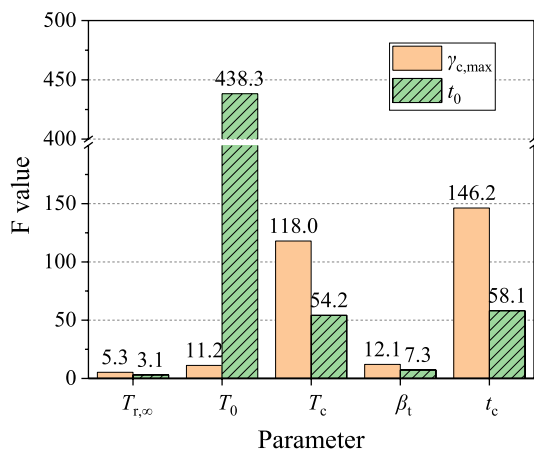
Fig. 18 Significant analysis of parameters

6 Spatio-temporal pattern of CTR

To facilitate the thermal design of composite girder during hydration process, a spatio-temporal pattern of CTR consisting a vertical pattern and an evolutionary pattern was proposed in this section.

6.1 Vertical pattern of CTR

It has been observed from Figs. 10 and 11 that temperature differences in the concrete deck are significantly small,

and the generated self-stress in concrete deck can also be ignored. Therefore, for the simplification of the vertical pattern of CTR, it can be reasonably considered that the temperature is evenly distributed in the thickness direction of concrete deck. Previous analysis has also shown that the steel temperature of the bottom flange is only affected and almost equals to the curing temperature, based on which a simplified vertical pattern of CTR was subsequently proposed as shown in Fig. 19.

In the vertical pattern, γ_c is the uniform CTR of concrete deck. γ_{sd} is the CTR of the bottom flange of steel girder and can be calculated by assuming that the temperature at the bottom of the steel girder equals to the curing temperature. $\Delta\gamma$, which equals to γ_c minus γ_{sd}, is the difference of CTR in steel girder. n is the power exponent. h_0 is the influence height of hydration heat on steel girder. h_s is the height of steel girder. According to the relationship between h_s and h_0, the vertical pattern was divided into the following two categories:

- When $h_0 > h_s$, the vertical pattern is composited with a uniform section in concrete deck, a variable section with power curve in steel girder, and a uniform section in steel girder, as shown in Fig. 19a and expressed with Eq. (10).
- When $h_0 < h_s$, the uniform section in steel girder does not exist, only the uniform section in concrete deck and the partial variable section in steel girder remain, as shown in Fig. 19b and expressed with Eq. (11).
- When $h_s > h_0$,

$$\gamma(y) = \begin{cases} \gamma_c & y \leq 0 & \text{Uniform section in concrete deck} \\ \gamma_{sd} + \Delta\gamma \left(1 - \frac{y}{h_0}\right)^n & 0 < y \leq h_0 & \text{Variable section in steel girder} \\ \gamma_{sd} & h_0 < y \leq h_s & \text{Uniform section in steel girder} \end{cases} \tag{10}$$
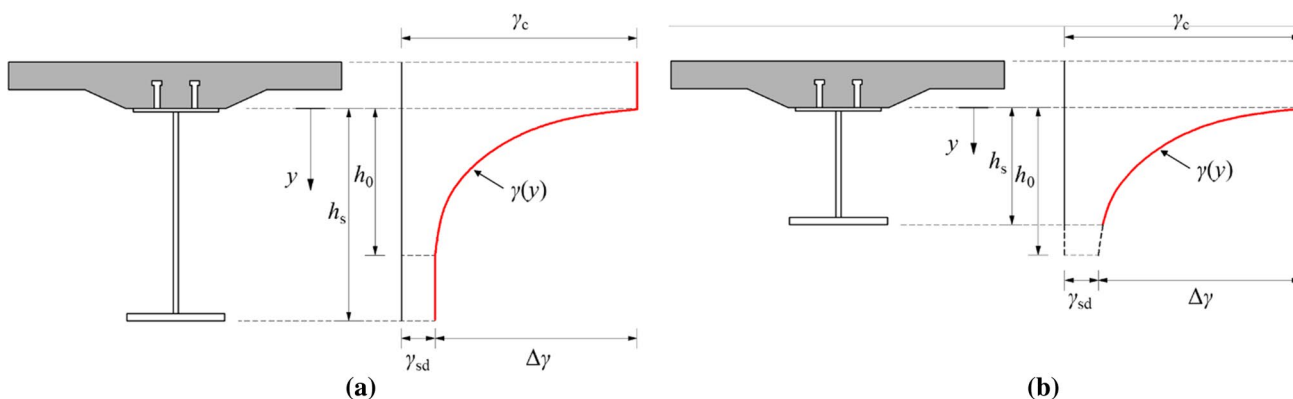

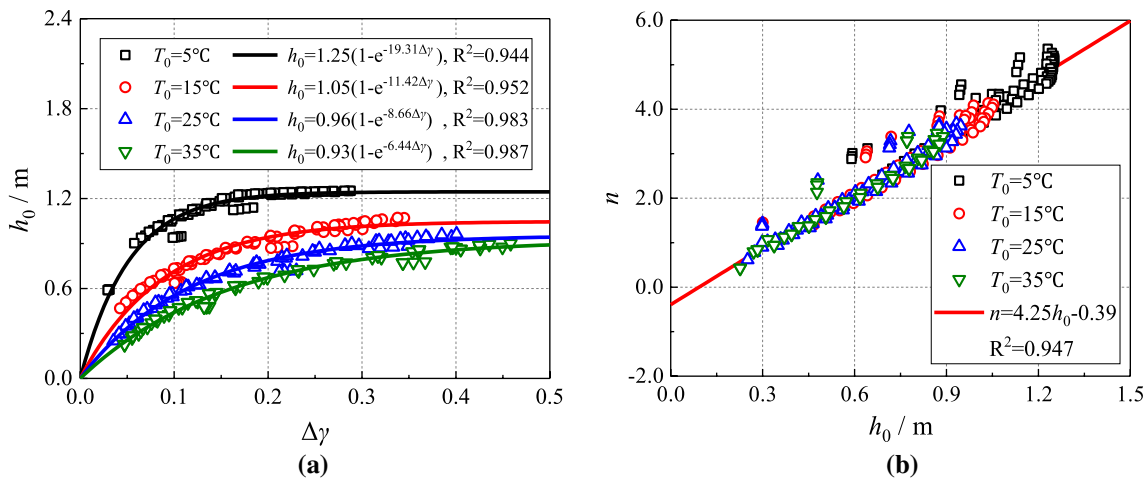**Fig. 19** Vertical patterns of TRC: **a** $h_s > h_0$, and **b** $h_s < h_0$

Fig. 20 Relationships between **a** h_0 and $\Delta\gamma$, and **b** n and h_0

- when $h_s < h_0$,

determine the corresponding h_0. n is independent of T_0 and increases linearly with the increase of h_0.

$$\gamma(y) = \begin{cases} \gamma_c & y \leq 0 \quad \text{Uniform section in concrete deck} \\ \gamma_{sd} + \Delta\gamma\left(1 - \dfrac{y}{h_0}\right)^n & 0 < y \leq h_s \quad \text{Variable section in steel girder} \end{cases} \tag{11}$$

In the proposed vertical pattern, obviously, the influence height h_0 can be expressed as the function of $\Delta\gamma$, and n can be subsequently calculated by h_0. Through regression of the results of parametric study, the calculation formulae of h_0 and n can be obtained as Eqs. (12) and (13). Figure 20 also shows their relationships. Among them, exponential relationships were shown between h_0 and $\Delta\gamma$ with $T_0 = 5$ °C, 15 °C, 25 °C and 35 °C. The larger the T_0, the smaller the h_0. For another T_0, interpolation method can be used to

$$h_0 = \begin{cases} 1.25\left(1 - e^{-19.31\Delta\gamma}\right) & T_0 = 5, \\ 1.05\left(1 - e^{-11.42\Delta\gamma}\right) & T_0 = 15, \\ 0.96\left(1 - e^{-8.66\Delta\gamma}\right) & T_0 = 25, \\ 0.93\left(1 - e^{-6.44\Delta\gamma}\right) & T_0 = 35, \end{cases} \tag{12}$$
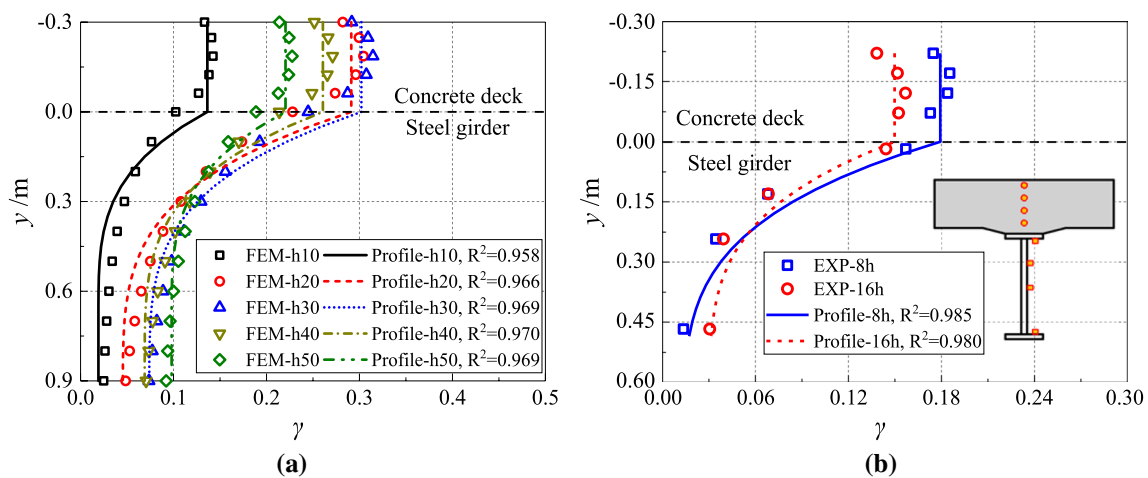
$$n = 4.25h_0 - 0.39 \tag{13}$$

Fig. 21 Verification of the proposed vertical pattern of CTR with **a** 3D FEM and **2** Choi's experiment [9]

Figure 21 shows the verification of the proposed vertical patten. Both the CTR results of FEM and in Choi's [9, 10] experiments are in good agreement with the proposed patterns, and all the R^2 are larger than 0.95, which well verifies the accuracy and applicability of the proposed vertical pattern. Based on the pattern, vertical temperature distributions can be obtained by only knowing the historical temperature evolutions of concrete deck and curing temperature. In addition, this pattern is independent of concrete age, as well can significantly reduce the number of sensors for the temperature measurement of composite girder during hydration process.

6.2 Evolutionary pattern of CTR

Measured temperature evolution of concrete deck is generally not available at the design stage. A simple method for the fast calculation of the temperature evolution of bridge deck is required. However, no readymade method is provided in the current specification system. Through measurement and FEM analysis, it was found that the evolutionary pattern of the CTR of concrete deck with age can be expressed by two "S" curves: ascending stage and descending stage, as shown in Fig. 22 and expressed with Eq. (14).

$$\gamma_c(t) = \begin{cases} \dfrac{\gamma_{c,\max}}{1+\left(\dfrac{t_0-t}{t_0-t_1}\right)^p}, & t \leq t_0, \text{ Ascending stage} \\ \dfrac{\gamma_{c,\max}-\gamma_{T_c}}{1+\left(\dfrac{t-t_0}{t_2-t_0}\right)^q} + \gamma_{T_c}, & t > t_0, \text{ Descending stage} \end{cases} \quad (14)$$

where $\gamma_c(t)$ is the CTR of concrete deck. $\gamma_{c,\max}$ is the maximum value of $\gamma_c(t)$. γ_{T_c} is the CTR after the hydration heat is over, $\gamma_{T_c} = (T_c - T_0)/T_{r,\infty}$. t_0 is the corresponding age to $\gamma_{c,\max}$. t_1 and t_2 are the corresponding ages to $\gamma_{c,\max}/2$ in ascending stage and $(\gamma_{c,\max} + \gamma_{T_c})/2$ in descending stage. p and q are coefficients.

Based on the FEM results, multiple regression analysis was performed to derive the parametric formulae of characteristic parameters, $\gamma_{c,\max}$ and t_0, in Eq. (14). The general functions adopted for regressions were all determined through repeated efforts. Through multiple regression
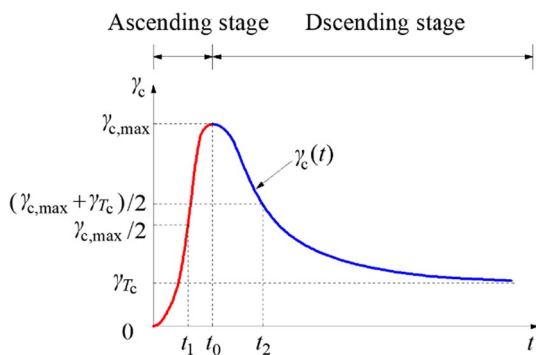
analysis, the proposed formulae for $\gamma_{c,\max}$ and t_0 were achieved and shown in Eqs. (15) and (16) with the five basic parameters $T_{r,\infty}$ in °C, T_0 in °C, T_c in °C, β_t in kJ/m² h °C and t_c in m. In addition, with $\gamma_{c,\max}$ and t_0, the empirical formulae of t_1 and t_2 were also established as Eqs. (17) and (18). Also, it was found that the five parameters had little influence on p and q. Thus, the average value of regression results was taken as the value of p and q, i.e., $p = 5.69$, $q = 2.09$.

$$\gamma_{c,\max} = (T_0 - T_c)\left(T_{r,\infty}^{0.012} - 1.057\right) + T_c^{0.069} - 0.005\beta + \left(-1.212t_c^2 + 1.471t_c\right) - 1.155 \quad (15)$$

$$t_0 = 17.154e^{0.0002T_{r,\infty}(T_0-T_c)-0.046T_0+0.022T_c-0.011\beta+\left(-2.496t_c^2+3.201t_c\right)} \quad (16)$$

$$t_1 = 1.896 - 0.545\gamma_{c,\max}^{0.501} + 0.301t_0^{1.237} - 0.233\gamma_{c,\max}^{0.501}t_0^{1.237} \quad (17)$$

$$t_2 = 3.715 + 3.745\left(\gamma_{c,\max} - \gamma_{T_c}\right)^{1.846} + 1.536t_0^{1.049} + 3.021\left(\gamma_{c,\max} - \gamma_{T_c}\right)^{1.846}t_0^{1.049} \quad (18)$$

For the purpose of checking the accuracy of the proposed formulae, comparisons of $\gamma_{c,\max}$, t_0, t_1 and t_2 between the predict values of the proposed formulae and FEM values of FEM analysis were carried out and shown in Fig. 23. In addition to R^2, the average absolute error (AAE) and the root-mean-square error (RMSE) [35] were also used to check the accuracy of the proposed formulae. For $\gamma_{c,\max}$, t_0, t_1 and t_2, all the R^2 exceed 0.97. Furthermore, the AAEs are only 0.015, 0.556 h, 0.246 h and 1.385 h, and the RMSEs are only 0.019, 0.667 h, 0.336 h and 1.724 h for $\gamma_{c,\max}$, t_0, t_1 and t_2. All the results indicate good accuracies and reliabilities of the proposed formulae.

Figure 24 shows the comparisons of CTR evolution between the proposed patterns (plotted in lines) and FEM results (plotted in scatters) in some parametric cases. All the R^2 of the comparisons exceed 0.97, verifying good accuracies and reliabilities. The proposed evolutionary pattern is a more efficient method and can be an approximate substitutionof FEM and experiment for the determination of the temperature evolution of concrete deck during hydration process. It also should be noted that this proposed evolutionary pattern was established to be applicable to a stationary curing temperature.

7 Thermal stress analysis

7.1 Simplified method for thermal stress calculation

This section presents a simplified method for the thermal stress calculation of composite girder with the proposed

Fig. 22 Evolutionary pattern of CTR of concrete deck
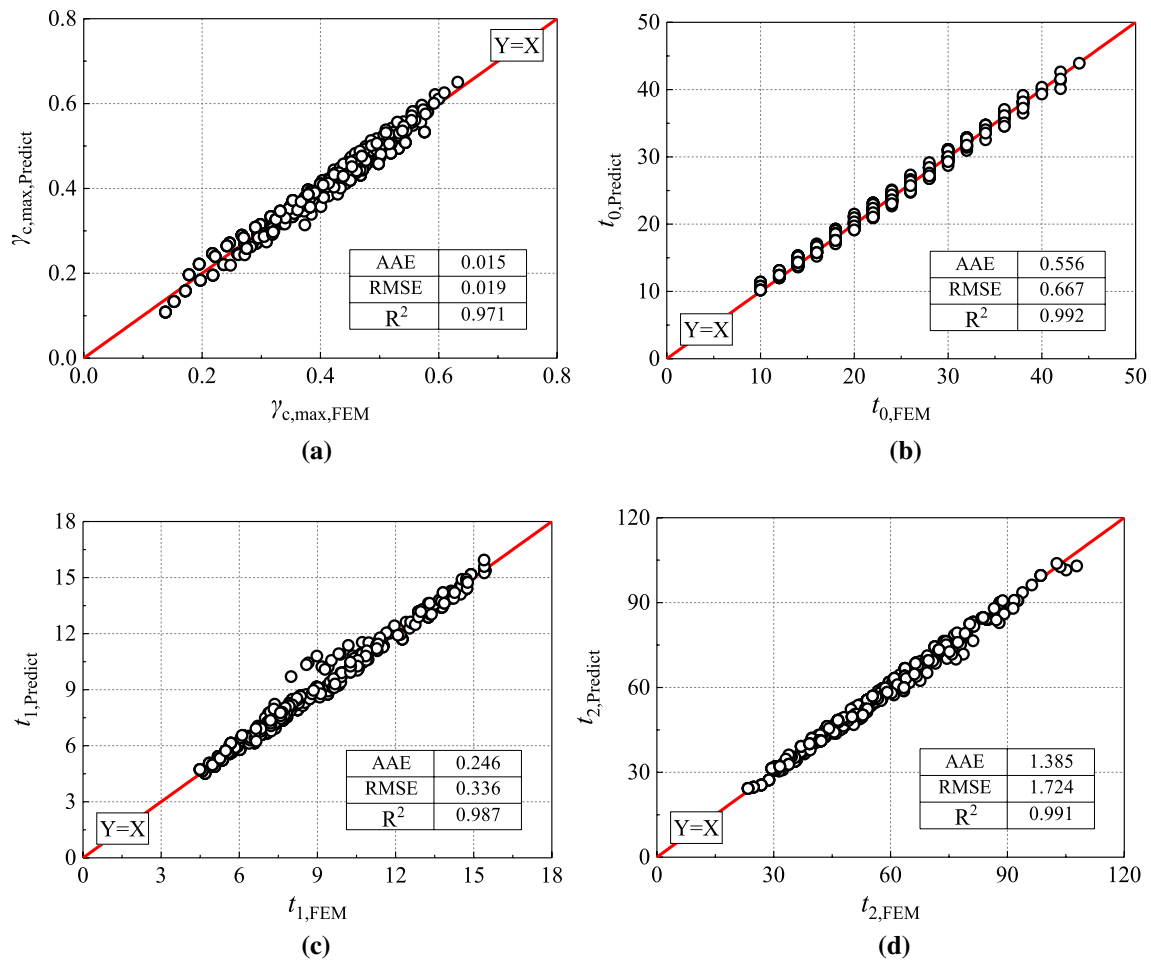
Fig. 23 Comparison between predicted value and FEM value of: **a** $\gamma_{c,max}$, **b** t_0, **c** t_1 and **d** t_2

spatio-temporal pattern of CTR. As well known, mechanical properties of concrete develop in time during the hydration process [23]. Therefore, an incremental analysis procedure was performed at a time step $\Delta t_i = t_i - t_{i-1}$. Additionally, the following limitations were also considered in the simplified method: (a) without regard to creep and shrinkage effect; (b) full interaction between concrete deck and steel girder, which means that the Euler–Bernoulli hypothesis is valid for the whole composite section; (c) the origin of y coordinate axis at the concrete–steel interface. Based on the above limitations, the increment of total axial strains $\Delta\varepsilon_{tot,i}(y)$ at Δt_i must satisfy

$$\Delta\varepsilon_{tot,i}(y) = \Delta\varepsilon_{0,i} + \Delta\varphi_i\left(y - y_{iG}\right) = \Delta\varepsilon_{e,i}(y) + \Delta\varepsilon_{T,i}(y) \quad (19)$$

where y_{iG} is distance from the centroid of composite section to the interface. $\Delta\varepsilon_{0,i}$ is the increment of centroidal axial strain. $\Delta\varphi_i$ is the increment of curvature. $\Delta\varepsilon_{e,i}$ is the increment of elastic strain, which result in stresses. $\Delta\varepsilon_{T,i}$ is the temperature strain and can be calculated by:

$$\Delta\varepsilon_{T,i}(y) = \alpha(y)\Delta T_i(y) \quad (20)$$

where $\alpha(y)$ is the coefficient of thermal expansion, and refers to α_c and α_s for concrete and steel, respectively. $\Delta T_i(y)$ is the vertical distribution of the temperature increment caused by hydration heat and can by calculated in terms of the proposed spatio-temporal pattern of CTR for an arbitrary parametric case. $\Delta T_{c,i}$ denotes the temperature increment of concrete, and $\Delta T_{s,i}(y)$ denotes the vertical distribution of the temperature increment of steel girder.

$$\Delta T_i(y) = T_{r,\infty}\left[\gamma_i(y) - \gamma_{i-1}(y)\right] \quad (21)$$

During hydration process, if no external forces are applied on the composite section, the centroidal axial force ΔN_i and the moment around the centroidal axis ΔM_i equals to zero. Then, the following equilibrium equations hold:

$$\Delta N_i = \int_{A_c+A_s} E_i(y)\left[\Delta\varepsilon_{0,i} + \Delta\varphi_i\left(y - y_{iG}\right) - \Delta\varepsilon_{T,i}(y)\right]dA = 0 \quad (22)$$
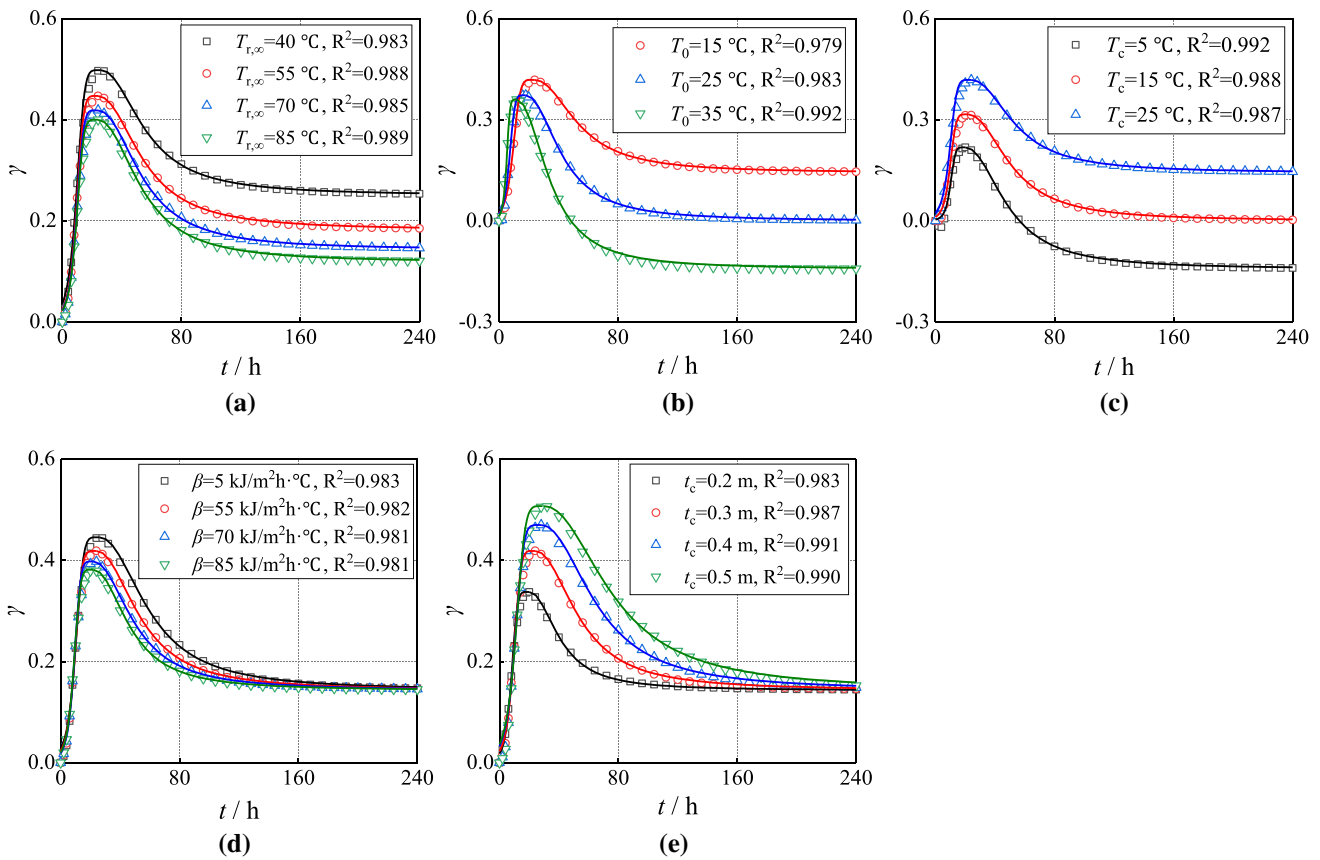
Fig. 24 Verification of the proposed evolutionary pattern of CTR in parametric case: **a** $T_0 = 15$ °C, $T_c = 25$ °C, $\beta_t = 10$ kJ/m² h °C and $t_c = 0.3$ m, **b** $T_{r,\infty} = 70$ °C, $T_c = 25$ °C, $\beta_t = 10$ kJ/m² h °C and $t_c = 0.3$ m, **c** $T_{r,\infty} = 70$ °C, $T_0 = 15$ °C, $\beta_t = 10$ kJ/m² h °C and $t_c = 0.3$ m, **d** $T_{r,\infty} = 70$ °C, $T_0 = 15$ °C, $T_c = 25$ °C and $t_c = 0.3$ m, **e** $T_{r,\infty} = 70$ °C, $T_0 = 15$ °C, $T_c = 25$ °C, and $\beta_t = 10$ kJ/m² h °C

$$\Delta M_i = \int_{A_c + A_s} E_i(y)\left[\Delta\varepsilon_{0,i} + \Delta\varphi_i(y - y_{iG}) - \Delta\varepsilon_{T,i}(y)\right](y - y_{iG})\mathrm{d}A = 0 \tag{23}$$

where A_c and A_s are the areas of concrete deck and steel girder. $E_i(y)$ is the elastic modulus and denotes $E_{c,i}$ for concrete at t_i and E_s for steel. CEB-FIP 2010 [36] provides the development of elastic modulus $E_{c,i}$ and tensile strength $f_{t,i}$ with the age and temperature for normal weight concrete as

$$E_{c,i} = E_{c,28}(1.06 - 0.003T)\left\{\exp\left[s\left(1 - \sqrt{\frac{28}{t_i}}\right)\right]\right\}^{0.5} \tag{24}$$

$$f_{t,i} = f_{t,28}(1.16 - 0.008T)\left\{\exp\left[s\left(1 - \sqrt{\frac{28}{t_i}}\right)\right]\right\}^{2/3} \tag{25}$$

where $E_{c,28}$ and $f_{t,28}$ is concrete's elastic modulus and tensile strength at an age of 28 days and a reference temperature of 20 °C. T is the temperature in °C. t_i is the age of concrete in day. s is a coefficient and depends on the type of cement.

By defining $\eta_i = E_{c,i}/E_s$, $\Delta\varepsilon_{0,i}$ and $\Delta\varphi_i$ in Eq. (19) can be solved as:

and $t_c = 0.3$ m, **c** $T_{r,\infty} = 70$ °C, $T_0 = 15$ °C, $\beta_t = 10$ kJ/m² h °C and $t_c = 0.3$ m, **d** $T_{r,\infty} = 70$ °C, $T_0 = 15$ °C, $T_c = 25$ °C and $t_c = 0.3$ m, **e** $T_{r,\infty} = 70$ °C, $T_0 = 15$ °C, $T_c = 25$ °C, and $\beta_t = 10$ kJ/m² h °C

$$\Delta\varepsilon_{0,i} = \frac{\eta_i \alpha_c \Delta T_{c,i} A_c + \alpha_s \int_{A_s} \Delta T_{s,i}(y)\mathrm{d}A}{\eta_i A_c + A_s} \tag{26}$$

$$\Delta\varphi_i = \frac{\eta_i \alpha_c \Delta T_{c,i} A_c y_{cG} + \alpha_s \int_{A_s} \Delta T_{s,i}(y)(y - y_{iG})\mathrm{d}A}{\eta_i I_{c,0} + I_{s,0}} \tag{27}$$

where y_{cG} is the coordinate of the centroid of concrete deck. $I_{c,0}$ and $I_{s,0}$ are the moments of inertia of the concrete deck and the steel girder around the centroidal axis of composite section.

With $\Delta\varepsilon_{0,i}$ and $\Delta\varphi_i$, the thermal stress increments of concrete deck and steel girder, $\Delta\sigma_{c,i}$ and $\Delta\sigma_{s,i}$ can be calculated by:

$$\Delta\sigma_{c,i}(y) = E_{c,i}\left[\Delta\varepsilon_{0,i} + \Delta\varphi_i(y - y_{iG}) - \alpha_c \Delta T_{c,i}\right] \tag{28}$$

$$\Delta\sigma_{s,i}(y) = E_s\left[\Delta\varepsilon_{0,i} + \Delta\varphi_i(y - y_{iG}) - \alpha_s \Delta T_{s,i}(y)\right] \tag{29}$$
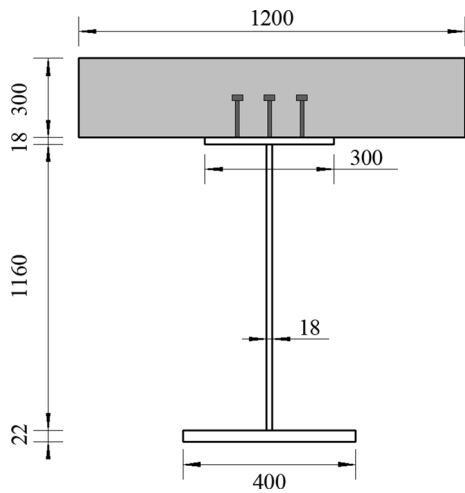
Fig. 25 Section dimensions of calculated composite girder (unit: mm)

7.2 Case study

In this section, a case study was performed on a composite girder with a C30 concrete deck. Figure 25 shows the section dimensions of the girder. Table 4 summarizes the relevant mechanical properties of C30 concrete and steel. Parametric cases that $T_{r,\infty} = 70$ °C, $T_0 = 25$ °C, $\beta_t = 5$ kJ/m^2 h °C, and $t_c = 0.3$ m in three curing temperature conditions of $T_c = 15$ °C, 20 °C and 25 °C were selected for the thermal stress calculation with the proposed simplified method.

Figure 26 depicts the calculated axial stress development in the concrete deck; the design value of tensile strength $f_{t,d}$ of C30 concrete was also plotted for comparison. It can be seen that when the curing temperature is 15 °C, the tensile stress of concrete starts to exceed $f_{t,d}$ at the time of 107 h, resulting in potential cracking risk in the concrete deck. When the curing temperature is increased to 20 °C and 25 °C, the tensile stress of concrete is always lower than $f_{t,d}$, and the cracking risk can be effectively controlled.

8 Discussion

The research in this paper is helpful to confirm that the early-age cracks mentioned by Darwin et al. [37] in the crack investigation of concrete deck. Subramaniam [8] observed the obvious temperature difference between the upper and lower flanges of the steel girder, believing that it contributed to the cracking of the concrete deck. Choi's [9, 10] test also suggested this temperature difference and also the large concrete–steel temperature difference. However, they did not clearly define the distribution patterns based on the temperature differences. This paper not only gives the spatial temperature pattern in the form of CTR, but also established the evolutionary pattern. As the case study implies, the effect of hydration heat on the early cracking risk in concrete deck can be efficiently estimated with the proposed spatio-temporal pattern of CTR and the simplified method for thermal tress calculation. As such, reasonable and effective curing schemes can be preliminarily and easily selected to control the early-age cracking in concrete before actual cast-in situ construction of concrete deck.

The analysis presented here is based on several simplifications, including full interaction between concrete deck and steel girder and uniform temperature of concrete deck, which were all issues that need further considerations for a finer and more accurate calculation of thermal stress.

9 Conclusions

This paper is aimed to propose a reasonable spatio-temporal pattern of hydration temperature and a simplified method to preliminarily and efficiently estimate the thermal stress of concrete deck during hydration process. The spatio-temporal pattern was established by using
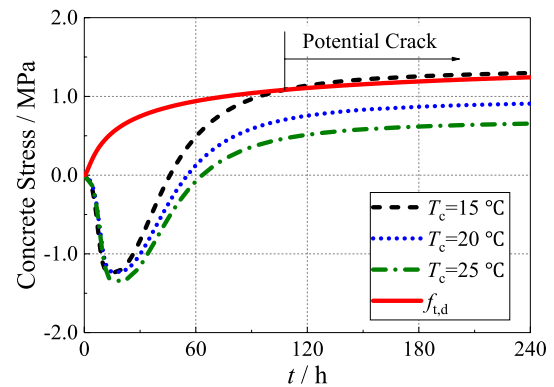

Fig. 26 Calculation of concrete stress with the proposed simplified method

Table 4 Mechanical properties

Mechanical property	C30concrete [38]	Steel
Elastic modulus, E (N/mm^2)	30,000 N/mm^2 at a 28-day age	206,000
Design value of tensile strength, $f_{t,d}$ (MPa)	1.39 MPa at a 28-day age	/
Characteristic value of tensile strength, $f_{t,k}$ (MPa)	2.01 MPa at a 28-day age	/
Coefficient of thermal expansion, α (1/°C)	1×10^{-5}	1.2×10^{-5}

finite-element models. These models were verified with large-scale temperament measurement on an actual composite girder bridge and then used to perform a comprehensive parametric study covering a wide range of basic parameters including $T_{r,\infty}$, T_0, T_c, β_t and t_c. Through multiple regression analysis, a series of empirical formulae was established to predict the key coefficients in the patterns. Based on the current investigation, main conclusions were drawn as follows:

1. Experiment shows that during hydration process, the temperature difference of concrete deck varied slowly within about 5 °C, significantly smaller than the temperature difference of entire composite section. The bottom flange temperature of steel girder basically changes in accordance with the curing temperature.

2. With experimental results, the accuracy of heat transfer FEM is fully verified at aspects of temperature evolution, vertical distribution and field contours. The ratio of the effects of hydration heat, solar radiation and air convection on the temperature change is 32.0:1:− 15.5 in the warming phase by hydration heat, which suggests that the influence of solar radiation can be basically ignored.

3. The spatio-temporal pattern proposed in the form of CTR includes vertical patterns and an evolutionary pattern. The vertical patterns consist of a uniform section in concrete deck, a variable section with power curve in steel girder and a uniform section in steel girder. The evolutionary pattern can be expressed by two "S" curves in ascending and descending stages. The accuracies and reliabilities of these patterns were all properly verified with the results of experiments or FEMs.

4. The simplified method for the thermal stress calculation of concrete deck during hydration process is established based on an incremental analysis procedure with the proposed spatio-temporal pattern of CTR. As such, reasonable and effective curing schemes can be easily selected to control the early-age cracking in concrete before actual cast-in situ construction of concrete deck.

The simplified method proposed in this paper is based on the assumption of full interaction between concrete and steel and does not consider the effects of creep and shrinkage. Additionally, the self-stress caused by the nonlinear temperature distribution of concrete deck is not considered neither, although the temperature is nearly uniformly distributed in the concrete deck. These are all the further researches that should be carried out in the future.

Compliance with ethical standards

Conflict of interest The authors declare that they have no conflict of interest.

Ethical statement Authors state that the research was conducted according to ethical standards.

References

1. Noorzaei J, Bayagoob KH, et al. Thermal and stress analysis of Kinta RCC dam. Eng Struct. 2006;28:1795–802.
2. Honorio T, Bary B, Benboudjema F. Evaluation of the contribution of boundary and initial conditions in the chemo-thermal analysis of a massive concrete structure. Eng Struct. 2014;80:173–88.
3. Xia Y, Nassif H, Su D. Early-age cracking in high performance concrete decks of a curved steel girder bridge. J Aerospace Eng. 2016;30:B4016003.
4. Schmitt RT, Darwin D. Effect of material properties on cracking in bridge decks. J Bridge Eng. 1999;4:8–13.
5. Gara F, Leoni G, Dezi L. Slab cracking control in continuous steel-concrete bridge decks. J Bridge Eng. 2013;18:1319–27.
6. Lebet JP, Ducret JM. Early concrete cracking of composite bridges during construction. Compos Constr Steel Concr. 2000;4:13–24.
7. William GW, Shoukry SN, Riad MY. Early age cracking of reinforced concrete bridge decks. Bridge Struct. 2005;1:379–96.
8. Subramaniam KV, Kunin J, et al. Influence of early temperature rise on movements and stress development in concrete decks. J Bridge Eng. 2010;15:108–16.
9. Choi S, Cha SW, et al. Thermo-hygro-mechanical behavior of early-age concrete deck in composite bridge under environmental loadings. Part 1: temperature and relative humidity. Mater Struct. 2011;44:1325–46.
10. Choi S, Cha SW, et al. Thermo-hygro-mechanical behavior of early-age concrete deck in composite bridge under environmental loadings. Part 2: strain and stress. Mater Struct. 2011;44:1347–67.
11. Faria R, Azenha M, Figueiras JA. Modelling of concrete at early ages: Application to an externally restrained slab. Cement Concr Compos. 2006;28:572–85.
12. Huang Y, Liu G, et al. Experimental and finite element investigations on the temperature field of a massive bridge pier caused by the hydration heat of concrete. Constr Build Mater. 2018;192:240–52.
13. Lee Y, Kim JK. Numerical analysis of the early age behavior of concrete structures with a hydration based microplane model. Comput Struct. 2009;87:1085–101.
14. Zhang N, Liu Y, et al. Temperature effects of H-shaped concrete pylon in arctic-alpine plateau region. J Traffic Transp Eng. 2017;17:67–77 **(in Chinese)**.
15. American Association of State Highway and Transportation Officials. AASHTO LRFD Bridge Design Specification. Washington: AASHTO; 2017.
16. European Committee for Standardization. Eurocode 1, Actions on Structures, Part 1-5: General Actions-Thermal Actions. Brussels: European Committee for Standardization; 1991.
17. Liu Y, Liu J, Zhang N. Review on solar thermal actions of bridge structures. China Civ Eng J. 2019;52:59–78 **(in Chinese)**.
18. Priestley MJN. Design of concrete bridges for temperature gradients. J Am Concr Inst. 1978;75:209–17.
19. Liu J, Liu Y, et al. Long-term field test of temperature gradients on the composite girder of a long-span cable-stayed bridge. Adv Struct Eng. 2019;22:2785–98.

20. Song Z, Xiao J, Shen L. On temperature gradients in high-performance concrete box girder under solar radiation. Adv Struct Eng. 2012;15:399–415.

21. Liu J, Liu Y, Zhang G. Experimental analysis on temperature gradient patterns of concrete-filled steel tubular members. J Bridge Eng. 2019;24:04019109.

22. Zhang N, Zhou X, et al. In-situ test on hydration heat temperature of box girder based on array measurement. China Civ Eng J. 2019;52:76–86 **(in Chinese)**.

23. Bertagnoli G, Gino D, Martinelli E. A simplified method for predicting early-age stresses in slabs. Eng Struct. 2017;140:286–97.

24. Louche A, Cristofari C, Notton G. Study of the thermal behaviour of a production unit of concrete structural components. Appl Therm Eng. 2004;24:1087–101.

25. Zhang Z, Wang K, et al. Study of influential factors of hydration heat and surface cracking resistance of concrete pier in construction. Bridge Constr. 2015;45:65–70 **(in Chinese)**.

26. Li D, Maes MA, Dilger WH. Thermal design criteria for deep prestressed concrete girders based on data from confederation bridge. Can J Civ Eng. 2004;31:813–25.

27. Tong M, Tham LG, Au FTK. Extreme thermal loading on steel bridges in tropical region. J Bridge Eng. 2002;7:357–66.

28. Liu J, Liu Y, et al. Vertical temperature gradient pattern of " 上"-shape steel-concrete composite girder in arctic-alpine region. J Traffic Transp Eng. 2017;17:32–44 **(in Chinese)**.

29. Zhu BF. Thermal stresses and temperature control of mass concrete. 1st ed. Oxford: Butterworth-Heinemann; 2013.

30. Zhang J, Xu X, Liu W. A test study on the solar radiation absorption coefficient of concrete surface. Build Sci. 2006;22:42–5.

31. Liu H, Chen Z, et al. Studies on the temperature distribution of steel plates with different paints under solar radiation. Appl Therm Eng. 2014;71:342–54.

32. Ministry of Housing and Urban-Rural Development of P.R. China. Code for construction of concrete structures, GB 506666-2011. Beijing: China Building Industry Press; 2011. **(in Chinese)**.

33. Matteis DD. Steel–concrete composite bridges sustainable design guide. Paris: Transport Studies Service; 2010.

34. Montgomery DC. Design and analysis of experiments. 9th ed. New York: Wiley; 2017.

35. Abid SR, Taysi N, Ozakca M. Experimental analysis of temperature gradients in concrete box-girders. Constr Build Mater. 2016;106:523–32.

36. CEB-FIP. Model code for concrete structures. London: Thomas Telford; 2010.

37. Darwin D, Browning J, Lindquist WD. Control of cracking in bridge decks: observations from field. Cem Concr Aggreg. 2004;26:148–54.

38. Ministry of Transport of P.R. China. Specifications for design of highway reinforced concrete and prestressed concrete bridges and culverts, JTG 3362-2018. Beijing: China Communications Press; 2018. **(in Chinese)**.

Publisher's Note Springer Nature remains neutral with regard to jurisdictional claims in published maps and institutional affiliations.